Dalton Transactions

PAPER

View Article Online
View Journal | View Issue

Cite this: *Dalton Trans.*, 2017, **46**, 12544

Electronic and molecular structure relations in diiron compounds mimicking the [FeFe]-hydrogenase active site studied by X-ray spectroscopy and quantum chemistry†

Ramona Kositzki,[a] Stefan Mebs,[a] Nils Schuth,[a] Nils Leidel,[a] Lennart Schwartz,[b] Michael Karnahl, ‡[b] Florian Wittkamp,[c] Daniel Daunke,[d] Andreas Grohmann,[d] Ulf-Peter Apfel, [c] Frédéric Gloaguen,[e] Sascha Ott [b] and Michael Haumann *[a]

Received 25th July 2017,
Accepted 7th September 2017

DOI: 10.1039/c7dt02720f

rsc.li/dalton

Synthetic diiron compounds of the general formula $Fe_2(\mu\text{-}S_2R)(CO)_n(L)_{6-n}$ (R = alkyl or aromatic groups; L = CN^- or phosphines) are versatile models for the active-site cofactor of hydrogen turnover in [FeFe]-hydrogenases. A series of 18 diiron compounds, containing mostly a dithiolate bridge and terminal ligands of increasing complexity, was characterized by X-ray absorption and emission spectroscopy in combination with density functional theory. Fe K-edge absorption and Kβ main-line emission spectra revealed the varying geometry and the low-spin state of the Fe(I) centers. Good agreement between experimental and calculated core-to-valence-excitation absorption and radiative valence-to-core-decay emission spectra revealed correlations between spectroscopic and structural features and provided access to the electronic configuration. Four main effects on the diiron core were identified, which were preferentially related to variation either of the dithiolate or of the terminal ligands. Alteration of the dithiolate bridge affected mainly the Fe–Fe bond strength, while more potent donor substitution and ligand field asymmetrization changed the metal charge and valence level localization. In contrast, cyanide ligation altered all relevant properties and, in particular, the frontier molecular orbital energies of the diiron core. Mutual benchmarking of experimental and theoretical parameters provides guidelines to verify the electronic properties of related diiron compounds.

Introduction

Hydrogen (H_2) is a promising fuel for a future economy based on sustainable energy sources.[1–3] Efficient proton reduction catalysts based on cheap and earth-abundant transition metals would represent a step forward towards the ubiquitous use of H_2.[4–7] The most efficient H_2 conversion catalysts in nature are the [FeFe]-hydrogenases, which possess an iron cofactor (H-cluster).[8–10] The H-cluster consists of a [4Fe4S] cubane linked to a diiron unit, the latter being the active site of H_2 turnover. Its two iron ions bind carbon monoxide (CO) and cyanide (CN^-) ligands, as well as a dithiolate bridge containing a pendant amine base (Fig. 1).[11–14] The strong-field CO/CN^- ligands bias the iron ions towards the low-spin state and they likely shuttle between Fe(I) and Fe(II) in the reaction cycle.[15,16] The specific roles of the diatomic ligands, the dithiolate bridge, and the cofactor geometry in the catalytic reactions are not fully understood so far.

Synthetic chemistry has produced a wealth of model compounds of the diiron unit with the aim to create functional [FeFe]-hydrogenase mimics.[4,17–33] At least 300 diiron com-

[a]*Freie Universität Berlin, Fachbereich Physik, 14195 Berlin, Germany. E-mail: michael.haumann@fu-berlin.de; Tel: +49 30 838 56101*
[b]*University of Uppsala, Department of Chemistry, Ångström Laboratories, 75120 Uppsala, Sweden*
[c]*Ruhr-Universität Bochum, Anorganische Chemie I, 44801 Bochum, Germany*
[d]*Technische Universität Berlin, Institut für Chemie, Bioanorganische Chemie, 10623 Berlin, Germany*
[e]*CNRS, Université de Bretagne Occidentale, UMR 6521, 29238 Brest, France*

†Electronic supplementary information (ESI) available: Bond lengths in diiron compounds, K-edge and $K\beta_{1,3}$ line energies, fit parameters for calculated *vs.* experimental ctv and vtc energies and intensities, normalized iron parameters, schematic drawing of the structures of the diiron compounds, pre-edge absorption features in the XANES, experimental Kβ satellite emission spectra, iron and ligand contributions to ctv and vtc spectra from DFT, crystal structures and geometry-optimized structures, interatomic distances in **1–18** from crystal and relaxed structures, calculated ctv and vtc spectra for crystal and relaxed structures, Fe(d) character and energy of valence MOs, relation of normalized structural and electronic parameters, second derivative vtc and ctv spectra. See DOI: 10.1039/c7dt02720f

‡Present address: University of Stuttgart, Institute of Organic Chemistry, 70569 Stuttgart, Germany.

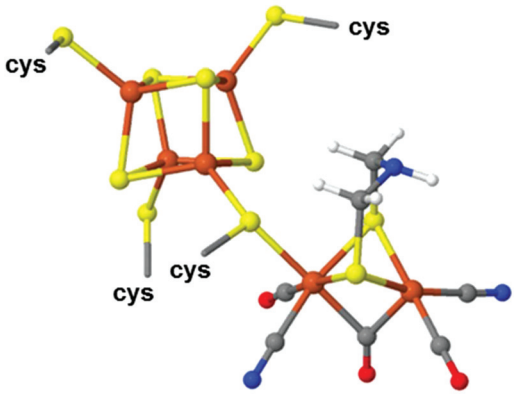

Fig. 1 Hydrogen-converting cofactor in [FeFe]-hydrogenase. The shown crystal structure (PDB entry 4XDC[12]) is for the oxidized H-cluster in a bacterial enzyme. Color code: C, grey; O, red; N, blue; S, yellow; Fe, orange; cys denotes cysteine amino acids of the protein.

plexes have been reported, which reproduce essential features of the natural cofactor, such as diatomic ligand binding, open coordination sites, and metal-bridging groups. Selective ligand exchange has been explored for example to vary the basicity and geometry of the two iron sites, and to stabilize vacancies for substrate interactions. Characterization of diiron compounds with bound hydride, as well as studies on redox chemistry, protonation reactions, and oxygen sensitivity, limiting the applicability of synthetic and natural systems,[34,35] are a further research focus.[18,27,36–50] A better understanding of the protonation of diiron systems is important as many compounds tend to form an unreactive Fe–Fe bridging hydride, from which H_2 formation often requires considerable overpotentials.[51–56] A diiron compound working fully reversibly and close to the thermodynamic limit, like the natural system, has not yet been obtained. More rigorous analysis of the effects of ligand variations and geometry changes on the atomic-level physical properties of the compounds may help to improve this situation. In this study, 18 diiron compounds were analyzed, which show varying terminal ligands and substitutions at the bridging dithiolate molecule, as well as symmetry alterations.

Advanced X-ray absorption and emission spectroscopy techniques (XAS, XES) in concert with quantum chemical computations provide access to electronic features of metal complexes.[37,57–67] However, a combination of these methods has relatively rarely been applied to [FeFe]-hydrogenase mimics.[38,39,44,68–73] The K-edge absorption reflects the redox state and transitions into unoccupied molecular orbitals. The pre-edge absorption is due to resonant 1s core electron excitation into unoccupied orbitals (core-to-valence transitions, ctv) with selection-rule weighted transition probabilities. The ctv provides information on the energy distribution of unoccupied valance levels. The Kβ main-line emission stems from radiative decay of 3p electrons to the 1s hole. Line splitting into the $K\beta_{1,3}$ and Kβ′ features due to 3p/3d-spin exchange coupling renders it sensitive to the metal spin state. The $K\beta_{2,5}$ and Kβ″ features of the Kβ satellite emission are due to valence electron decay to the core hole (valence-to-core transitions, vtc) and probe occupied valence levels. The use of XAS/XES and crystal structures to benchmark density functional theory (DFT) results of spectral simulations is expected to provide detailed relations between structural and electronic features.

Here, we present a systematic study on an extended series of diiron compounds of increasing complexity using XAS/XES and DFT. Fe K-edge absorption variations were related to geometry changes at the Fe(I) centers, for which Kβ main-line emission spectra revealed the low-spin state. Good agreement of experimental and calculated pre-edge absorption (ctv) and Kβ satellite emission (vtc) spectra was obtained, revealing correlations between molecular and electronic parameters. Variation of the dithiolate bridge mainly affects the Fe–Fe distance, while an asymmetric donor substitution decreases the metal charge and enhances the valence delocalization. Cyanide ligation, like in the natural paragon, effectively alters most electronic properties of the diiron core.

Materials and methods

Synthesis of compounds and sample preparation

Compounds **1–18** were synthesized as described earlier (see Fig. 2 and Table 1 for references). Powder (microcrystalline) material of compounds **1–18** was homogeneously diluted by grinding with boron nitride (1 : 10 to 1 : 20) in an anaerobic chamber. The resulting samples were loaded into Kapton-covered acrylic-glass holders for XAS/XES and immediately frozen in liquid nitrogen.

X-ray absorption and emission spectroscopy

XAS/XES spectra at the Fe K-edge were collected at the triple-undulator beamline ID26 at the European Synchrotron Radiation Facility (ESRF, Grenoble, France).[38,39,68,74,75] Samples were held at 20 K in a liquid-He cryostat (Cryovac). The excitation energy was set by a Si[311] double-crystal monochromator (energy bandwidth ~0.2 eV). The spot size on the samples was shaped by slits to *ca.* 0.2 mm in vertical and 0.3–0.5 mm in horizontal. Fe K-edge absorption spectra were collected using the rapid scan mode of ID26 (scan duration ~5 s). The total (Kα) X-ray fluorescence was monitored with a scintillation detector shielded by 10 μm Mn foil against scattered X-rays. Fluorescence-detected K-edge spectra were corrected for minor flattening effects using the simultaneously measured transmission spectra.[76] A vertical-plane Rowland-circle spectrometer and an avalanche photodiode (APD) detector were used for monitoring of the non-resonantly (7600 eV) excited Kβ X-ray fluorescence. An energy bandwidth of ~1.0 eV at the Fe Kβ fluorescence lines was achieved using the Ge[620] Bragg reflections of 5 spherically-bent Ge wafers (R = 1000 mm). The energy axis of the monochromator was calibrated at an accuracy of ±0.1 eV using the K-edge spectrum of a Fe metal foil (fitted reference energy of 7112 eV in the first derivative spectrum). The energy axis of the emission spectrometer was cali-

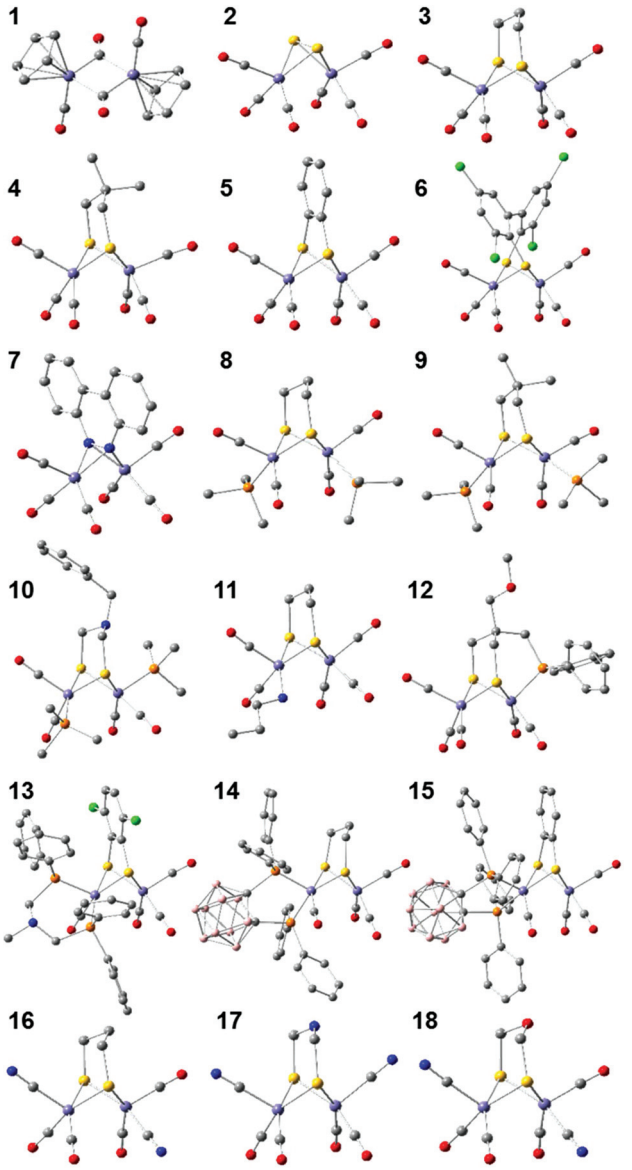

Fig. 2 Crystal structures of diiron compounds **1–18**. Color code: B, light-brown; C, grey; O, red; N, blue; P, orange; S, yellow; Cl, green; Fe, violet. Compound annotations: $Fe_2(\mu\text{-}CO)_2(Cp)_2(CO)_2$ (Cp = cyclopentadienyl, C_5H_5), **1**;[118] $Fe_2(\mu\text{-}S_2)(CO)_6$, **2**;[119] $Fe_2(\mu\text{-}pdt)(CO)_6$ (pdt = 1,3-propanedithiolate, $(SCH_2)_2CH_2$), **3**;[102] $Fe_2(\mu\text{-}dmpdt)(CO)_6$ (dmpdt = 2,2-dimethyl-pdt, $(SCH_2)_2C(CH_3)_2$), **4**;[120] $Fe_2(\mu\text{-}bdt)(CO)_6$ (bdt = benzene-1,2-dithiolate, $S_2C_6H_4$), **5**;[89,90] $Fe_2(\mu\text{-}Cl_4bpdt)(CO)_6$ (Cl_4bpdt = tetrachloro-biphenyl-2,2′-dithiolate, $S_2(C_6Cl_2H_2)_2$), **6**;[123] $Fe_2(\mu\text{-}bc)(CO)_6$ (bc = benzo[c]cinnoline, $N_2(C_6H_4)_2$), **7**;[124] $Fe_2(\mu\text{-}pdt)(CO)_4(PMe_3)_2$ (Me = CH_3), **8**;[125] $Fe_2(\mu\text{-}dmpdt)(CO)_4(PMe_3)_2$, **9**;[126] $Fe_2(\mu\text{-}(SCH_2)_2N(CH_2Ph))(CO)_4(PMe_3)_2$ (Ph = C_6H_5), **10**;[46] $Fe_2(\mu\text{-}pdt)(CO)_5(H_2NPr)$ (Pr = C_3H_7), **11**;[127] $Fe_2(\mu\text{-}dmpdt\text{-}OMe)(CO)_5(PPh_2)$, **12**,[128] $Fe_2(\mu\text{-}Cl_2bdt)(CO)_4(Ph_2PCH_2CH_3CH_2PPh_2)$, **13**;[129] $Fe_2(\mu\text{-}pdt)(CO)_4(BC)$ (BC = 1,2-bisdiphenylphosphine-1,2-*o*-carborane, $C_2B_{10}H_{10}$), **14**;[98] $Fe_2(\mu\text{-}bdt)(CO)_4(BC)$, **15**;[98] $[Fe_2(\mu\text{-}pdt)(CN)_2(CO)_4]^{2-}$, **16**;[130] $[Fe_2(\mu\text{-}adt)(CN)_2(CO)_4]^{2-}$ (adt = azadithiolate, $(SCH_2)_2NH$), **17**;[100] $[Fe_2(\mu\text{-}odt)(CN)_2(CO)_4]^{2-}$ (odt = oxodithiolate, $(SCH_2)_2O$), **18**.[99] Protons were omitted for clarity. See Fig. S1† for schematic drawings of the compound structures.

Table 1 Structural parameters of diiron compounds

Compound[a]	Number of CO ligands	Fe–Fe distance [Å]	Mean Fe–ligand bond length [Å]	CSD[b] code	Ref.
1	4	2.539	2.03	CYPFEC03	118
2	6	2.556	1.97	FOKCOX01	119
3	6	2.510	1.98	CAZMAR	102
4	6	2.494	1.99	VOFGUT	120
5	6	2.480	1.98	SIHXIQ	121 and 122
6	6	2.512	1.99	ERAMEQ	123
7	6	2.508	1.83	BCINFE	124
8	4	2.555	2.05	VOQCUZ	125
9	4	2.569	2.05	NONFAY	126
10	4	2.546	2.05	UCAYUT	46
11	5	2.552	2.00	XEPZEY	127
12	5	2.519	2.02	n.a.	128
13	4	2.531	2.07	CUTSAM	129
14	4	2.544	2.06	CEBBAO	98
15	4	2.497	2.06	CEBBES	98
16	4	2.518	1.99	WOLROE	130
17	4	2.509	2.00	YOBSEN	100
18	4	2.518	1.99	n.a.	99

[a] All compounds contain a formal Fe(I)Fe(I) core; [b] CSD = Cambridge Structural Database;[131] n.a., not available in the CSD.

brated at an accuracy of ±0.1 eV using a Gaussian fit to the elastic scattering peak of the energy-calibrated excitation beam. Kβ main line spectra were collected using spectrometer step-scanning (scan duration ~5 s, energy steps of 0.3 eV). About five spectra from separate sample spots were averaged for signal-to-noise ratio improvement and then normalized to unity area in a 7035–7075 eV range. Kβ satellite line emission spectra were collected using the previously described approach (energy step size 0.3 eV, 5 s data acquisition per sample spot, 5–7 data sets averaged).[77,78] A rapid shutter blocked the incident X-rays during emission spectrometer movements. XAS/XES data were processed and evaluated using our earlier described procedures and in-house software.[38,39,68,74,75,79] Pre-edge absorption spectra (ctv) were derived by polynomial background subtraction from normalized XANES spectra using in-house software. Kβ satellite emission spectra (vtc) were derived by subtraction of a smooth background accounting for the high-energy tail of the $K\beta_{1,3}$ line and normalization to unity area within 7075–7120 eV. Fits using 2 (ctv) or 6 (vtc) Gaussian functions with a variable full-width-at-half-maximum (FWHM) for the ctv spectra (same FWHM for the 2 peaks) or a fixed FWHM of 3.5 eV for the vtc spectra provided energies and intensities of experimental ctv and vtc peak features.

DFT calculations

Calculations were carried out on the Soroban computer cluster of the Freie Universität Berlin. Spin-unrestricted single-point DFT calculations on the crystal structures were carried out using the BP86/TZVPP functional/basis-set combination[80–82] as implemented in the ORCA program[83] to derive ctv and vtc stick spectra (*i.e.* transition intensities and energies) and MO energies, as well as MO metal/ligand characters of the com-

pounds.[38,75,76] For the two low-spin Fe(I) centers in all complexes, a total spin (S) of zero (multiplicity, $M = 2S + 1 = 1$) was favored by the lowest single-point energy of the structure in all cases. CM5 charges were calculated on the basis of geometry-optimized structures (BP86/TZVP, COSMO solvation model, ε = 4) using the Gaussian09 program.[84] Molecular orbitals were visualized with Gview.[84] For comparison with experimental spectra, calculated ctv sticks (in a range from the LUMO to ~3 eV) were shifted 181.9 eV on the energy axis, broadened by Gaussians (FWHM 0.8 eV), and resulting spectra were scaled (×165); calculated vtc sticks (in a range from ~7080 eV to the HOMO) were shifted by 181.3 eV on the energy axis, broadened by Lorentzians (FWHM 2.0 eV), and resulting spectra were scaled (×60). Calculated ctv spectra were fitted with 2 Gaussians (variable FWHM) and calculated vtc spectra were fitted with 6 Gaussians (FWHM 2.5 eV) as the experimental spectra to derive energies/intensities of ctv/vtc peaks.

Results

Structure of diiron compounds

The crystal structures of the diiron compounds are depicted in Fig. 2 and Fig. S1.† Selected metrical parameters are given in Table 1 and Table S1.† All compounds have a formal Fe(I)Fe(I) valence and exhibit increasing complexity, ranging from symmetric structures with all-carbonyl terminal iron ligation and no, small, or increasingly bulky bridging dithiolate or diamino groups (**1–7**), over structures with terminal ligand substitutions (*e.g.* by phosphine or cyanide) and small dithiolate groups (**8–11**, **16–18**), to asymmetric structures with diverse and bulky dithiolate groups and/or terminal groups such as a bisphosphine-carborane ligand (**12–15**). Despite the pronounced structure variations, the Fe–Fe distance deviated by maximally about ±0.05 Å from the mean value of 2.53 Å. Similarly, only moderate deviations (±0.12 Å) from the average iron–ligand bond length (~2.01 Å) were observed, although a larger bond-lengths spread was realized in the compounds with a more heterogeneous ligand environment. All complexes have 5-coordinated iron sites (except **1** with four ligands) carrying one to three CO and two μ-S ligands (except **7** with two μ-N ligands), as well as a variety of further ligand species (Fig. 2).

K-edge XAS and Kβ XES

XANES spectra at the Fe K-edge of the diiron compounds are shown in Fig. 3A. The spectra revealed pronounced shape variations due to changes in energy of unoccupied levels. The K-edge energy varied by almost 5 eV (~7120–7125 eV). Compounds **8–10** and **12–15** carrying phosphine or bisphosphine-carborane ligands at both Fe ions or only at one Fe ion showed lowest K-edge energies. **5–7** bearing phenyl or aryl groups at the dithiolate or diamino bridge showed highest energies. Compounds **16–18** binding CN^- ligands and **1** had intermediate energies. The edge energy of ferrous iron-oxide (*i.e.* Fe(II)O) was lower than that of the Fe(I)Fe(I) compounds. Kβ main-line emission spectra are shown in Fig. 3B. The

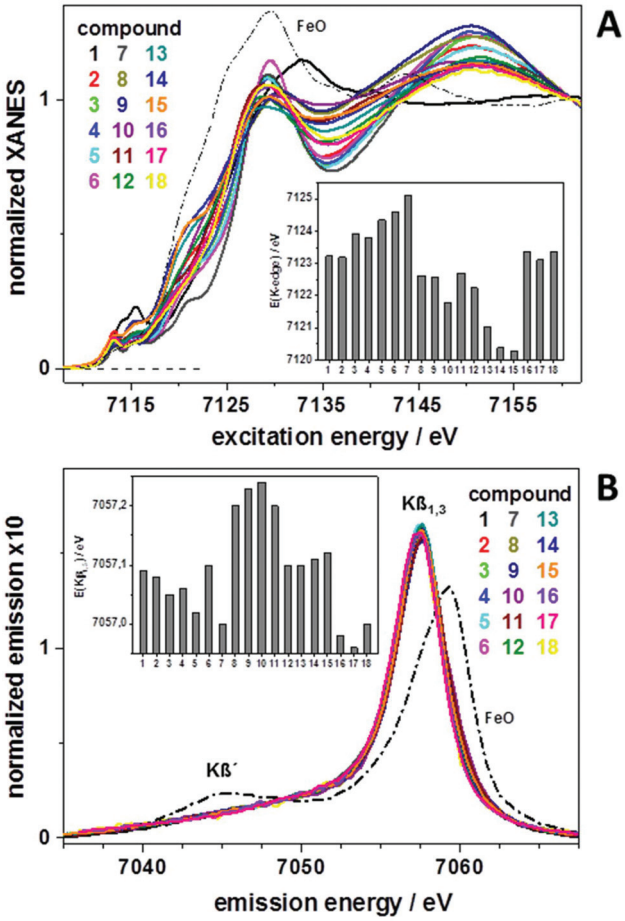

Fig. 3 Fe K-edge absorption and Kβ main-line emission spectra of **1–18**. (A) XANES spectra (inset, K-edge energies; see Fig. S2† for magnified pre-edge features). (B) Kβ main-line emission spectra (inset, $K\beta_{1,3}$ energies). Table S2† lists K-edge and $K\beta_{1,3}$ energy values. Spectra of Fe(II)O shown in (A) and (B) for comparison.

spectra appeared very similar for all compounds, showing a prominent $K\beta_{1,3}$ feature at ~7057 eV and a negligible Kβ′ feature at ~7045 eV. The small Kβ′ feature in comparison to the larger Kβ′ feature for high-spin Fe(II) in FeO indicates that the iron ions in all diiron complexes were in the low-spin state.[38,39,75,85,86] The $K\beta_{1,3}$ line energy varied by less than 0.3 eV. The complexes carrying, *e.g.*, phenyl or CN^- groups (**5–7**, **16–18**) had lower $K\beta_{1,3}$ energies whereas the complexes with, *e.g.*, phosphine or bisphosphine-carborane groups (**8–12**, **14**, **15**) had higher $K\beta_{1,3}$ energies. For an increase of the iron oxidation state by one unit in a comparable coordination environment, a shift of the K-edge by 2–3 eV to higher energies and a ~0.6 eV higher $K\beta_{1,3}$ energy is anticipated.[72,74,75,87–89] Therefore, the absolute K-edge energies and the variable energy changes between the compounds likely were dominated by the variations in the ligation environment of the diiron compounds, rather than being determined by changes in the iron redox state. Presumably, the altered coordination geometries at the iron centers affected the energy distribution of unoccupied levels. Rather similar $K\beta_{1,3}$ energies also imply

that the apparent iron oxidation state varied only slightly in the compounds and that the line energy changes mostly reflect the structural changes.[75,78,85]

Pre-edge absorption and Kβ satellite emission

Core-to-valence X-ray absorption spectra (ctv) and valence-to-core emission spectra (vtc) are shown in Fig. 4, 5 and Fig. S2, S3.† The ctv spectra revealed two apparent peak features with moderate intensity, bandwidth, and energy variations (Fig. 4A). In the vtc spectra, six apparent emission peak features were discernable, which vary in energy and shape (Fig. 5A). DFT calculations on the crystal structures yielded theoretical ctv and vtc spectra (Fig. 4B and 5B) that fairly well reproduce the differences between the experimental ctv and vtc spectra. Notably, very similar ctv/vtc spectra were calculated for geometry-optimized structures (Fig. S5–S7, Table S1†). Dissection of the characters of target molecular orbitals (MOs) for electronic excitation underlying the ctv spectra revealed that peak 1 is dominated by transitions into MOs with mostly

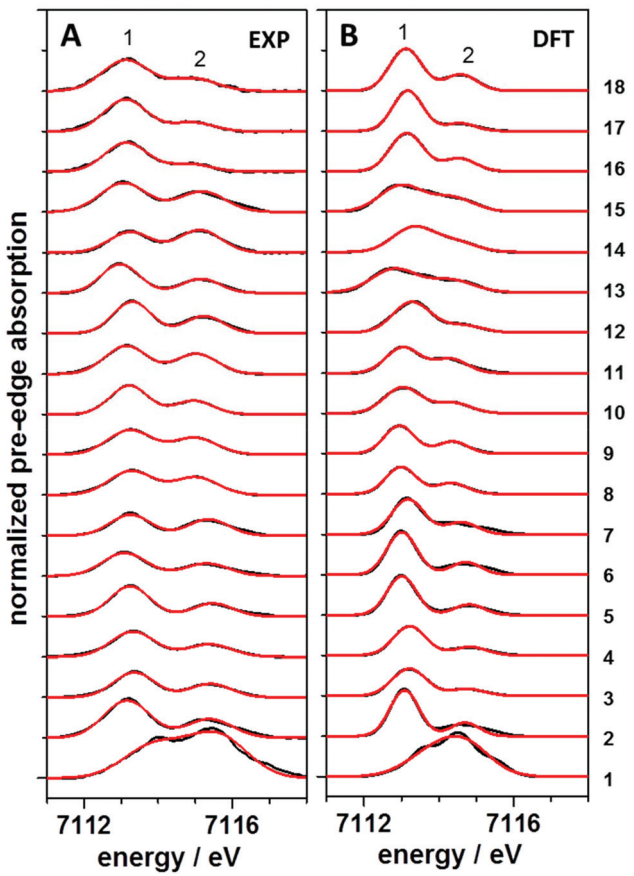

Fig. 4 Experimental and calculated Fe pre-edge absorption spectra of **1–18**. (A) Experimental ctv spectra derived after background subtraction from XANES data in Fig. 3A and Fig. S2.† (B) ctv spectra from DFT on crystal structures after Gaussian broadening of stick spectra. (A and B): Spectra of compounds indicated on the right; black lines, experimental data; red lines, fit curves with two Gausssians accounting for ctv peaks labeled 1 and 2 (top). Characters of target MOs for ctv electronic excitation transitions in (B) are shown in Fig. S4.†

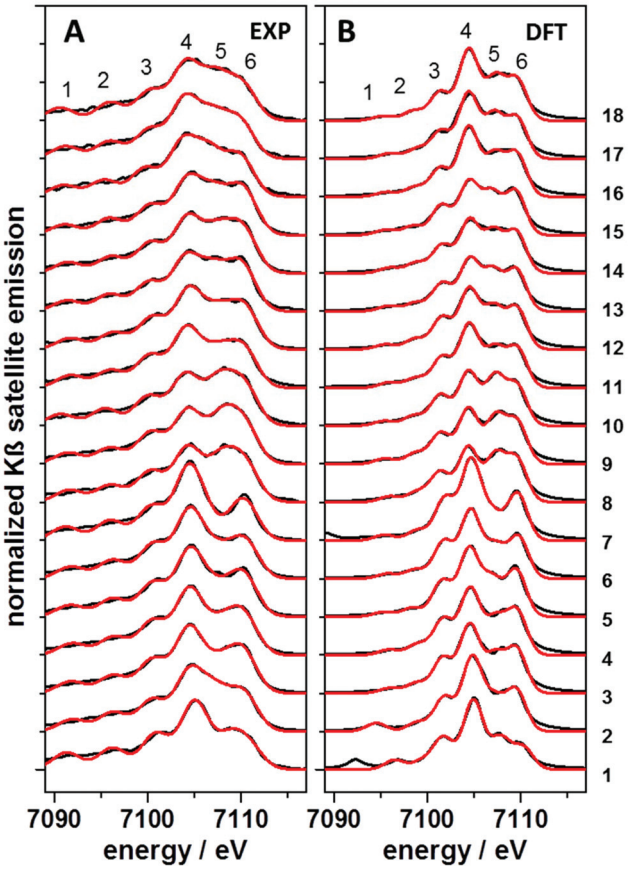

Fig. 5 Experimental and calculated Fe Kβ satellite emission spectra of **1–18**. (A) Experimental vtc spectra derived after subtraction of the background due to the high-energy tail of the $K\beta_{1,3}$ line (Fig. 3B and Fig. S3†). (B) Calculated vtc spectra from DFT on crystal structures after Lorentzian broadening of stick spectra. (A and B): Spectra of compounds indicated on the right; black lines, experimental data; red lines, fit curves with six Gausssians accounting for vtc peak features labeled 1–6 (top). Characters of source MOs for vtc electronic decay transitions in (B) are shown in Fig. S4.†

Fe and weak ligand character whereas peak 2 reflects transitions into MOs with mainly CO ligand character and minor Fe contributions (Fig. S4†). Dissection of the characters of source MOs for electronic decay underlying the vtc spectra revealed that peak 6 is dominated by MOs with mainly Fe character, peaks 1, 2, and 5 show major contributions from MOs mostly located at the bridging (dithiolate) groups and non-CO terminal ligands, while peaks 3 and 4 reflect transitions from CO-centered MOs (Fig. S4†).

For a more quantitative analysis, experimental and calculated ctv and vtc spectra were fitted with two or six Gaussian functions, which accounted for the visibly discernable spectral features (Fig. 4A, B and 5A, B). Correlations between the respective energies of all ctv/vtc peaks are shown in Fig. 6 (see Table S3† for correlations of individual ctv/vtc peaks). For the ctv spectra (Fig. 6A), the experimental and calculated energies of the two peaks agreed within margins of less than about ±0.2 eV for a mean energy difference of ~2 eV between the two

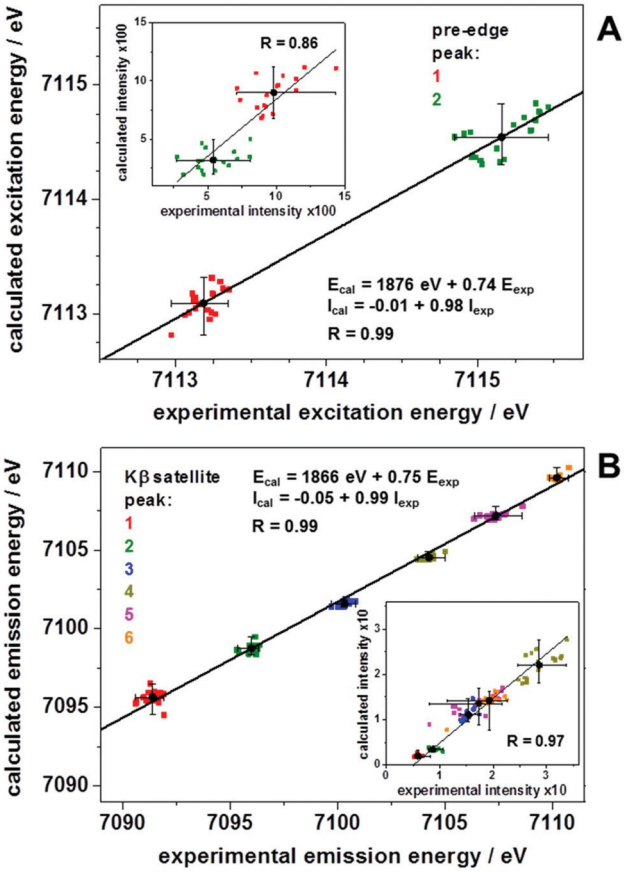

Fig. 6 Correlation of ctv and vtc transitions from experiment and DFT. (A) ctv energies (intensities in the inset). (B) vtc energies (intensities in the inset) corresponding to Gaussian fit functions in Fig. 4A, B (A) and Fig. 5A, B (B). (A and B): Black symbols and bars, mean values and full parameter ranges; straight lines, linear regressions with indicated parameters. Mean experimental ctv/vtc energy (relative intensity) errors are about ±0.1 eV (±10%). For correlations of energies/intensities of individual ctv/vtc peaks see Table S3.†

peaks. The correlation line slope revealed ~25% underestimation of the peak energy splitting, as previously observed for the chosen theory level.[38,39,69,70,74] This energy deviation is mostly attributable to the use of the general gradient approximation in the BP86 functional lacking Hartree–Fock exchange energy admixture,[90,91] but may contain contributions due to the use of only two ctv peaks in the analysis, as visible in the experimental ctv spectra. The peak intensities matched within about ±30% (reflecting, *e.g.*, limited accuracy of background subtraction from experimental data), but the correlation line slope was close to the ideal value of 1. The latter finding supported that the use of two peaks in the simulations was sufficient to reproduce the major spectral changes. For the vtc spectra (Fig. 6B), reasonable correlation between experimental and calculated energies for the six peaks within margins of less than ±0.5 eV for a mean energy difference of peaks 1 and 6 of ~20 eV and similar underestimation of energy differences were observed. Peak intensities matched within ±30% and the correlation line slope was close to 1. Relatively small energy and intensity changes in the ctv spectra implied that ligand exchange has a moderate effect on the energies of unoccupied valence MOs, as well as on the excitation transition probabilities. Larger changes in the vtc spectra suggested more pronounced differences in the energies of the occupied valence MOs and, in particular, varying decay contributions from MOs centered at the different ligands. MOs dominating the ctv/vtc transitions are exemplified for a symmetric and an asymmetric compound (**3** and **15**) in Fig. 7.

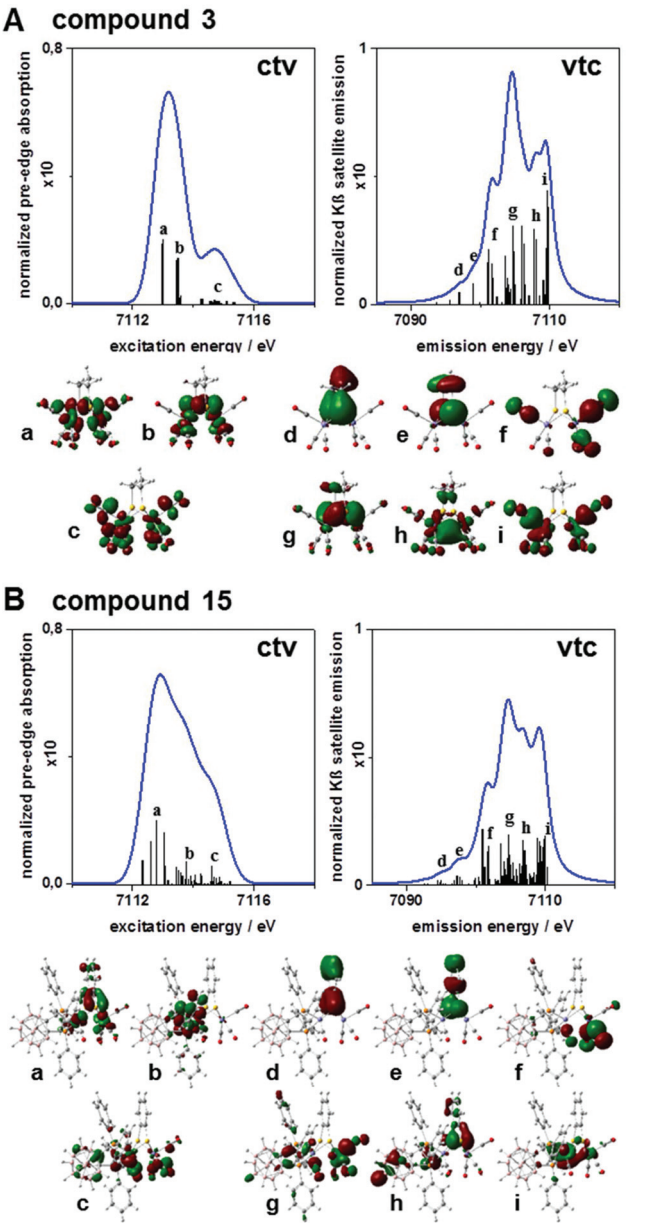

Fig. 7 Molecular orbitals involved in ctv and vtc transitions. Shown are ctv (left) and vtc (right) stick spectra from DFT, spectra after Gaussian (ctv) or Lorentzian (vtc) broadening of stick spectra, and corresponding selected target MOs for ctv excitation (labeled a–c) and source MOs for vtc decay (labeled d–i) for compound **3** (A) and compound **15** (B).

Consistent behavior in correlation plots of experimental or calculated ctv and vtc peak energies and amplitudes *versus* structural parameters of the diiron compounds emerged (Fig. 8). Linear fits, which were used as an approximation to the experimental and computational data, revealed similar slopes and *R* values for both sets of data (compare black and red lines in Fig. 8). Notably, the use of the mean Fe–ligand distance, which levels out the increased bond lengths spread in the more asymmetric compounds to some extent, may be the reason for a relatively weak correlation to the energies of the ctv peak features. These findings showed that the trends in the experimental data were reasonably reproduced by the computational approach. The energy of ctv peak 1 was unrelated to the Fe–Fe distance, which means that small differences in metal–metal bond strength do not systematically affect the energies of unoccupied valence MOs. An energy increase by ~0.5 eV of ctv peak 2 implies a shift of unoccupied MOs with dominant CO character to higher energies for an increase of the number of CO ligands from four to six (as in **16** *vs.* **5**). An overall energy decrease by ~0.5 eV of ctv peak 2 for a ~0.1 Å increase of the mean metal–ligand distance was compatible with the data and presumably reflects increasing contributions of non-CO ligands to unoccupied MOs (*e.g.* in **8–18**). The energy increase by ~0.5 eV and intensity increase by ~15% of vtc peak 3 for a change of the number of CO ligands from four to six is due to enhanced decay contributions from CO-centered MOs. A decrease by ~20% of the intensity of ctv peak 4 for a mean metal–ligand bond elongation by ~0.1 Å is consistent with diminished decay probabilities from respective ligand-centered occupied MOs.

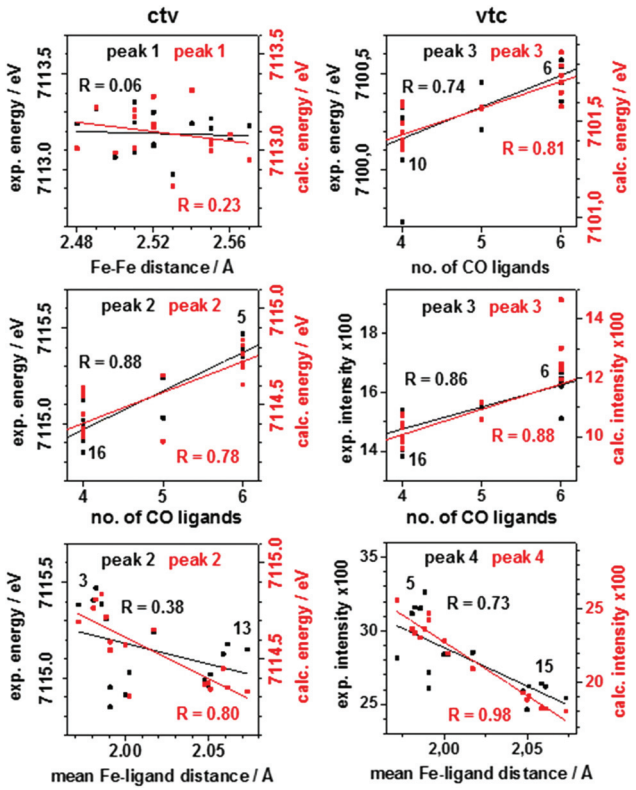

Fig. 8 Correlation of structural features and ctv/vtc spectra for **1–18**. Data from experiment (exp., black symbols and lines, left *y*-axis) and DFT (calc., red symbols and lines, right *y*-axis) and linear fits (lines). Energies and intensities of ctv (left panels) and vtc (right panels) peaks correspond to data in Fig. 6. Selected compounds with parameter values at the extremes are indicated. Data for **1** and **7** were omitted from the analysis.

Charge distribution

DFT was used to calculate CM5 charges on the iron ions and the ligands (Fig. 9). The mean summed charge on the iron centers was ~0.7. A smaller charge on iron for **8–10** and **13–18**, a larger charge for **2–6** and **11–12**, and maximal charges for **1** with bridging CO ligands and for **7** with a diamino bridge were found. Both iron ions were about equally charged, except for compounds **13–15** with an asymmetric ligation sphere at the two iron centers, which showed asymmetric charging due to less positive charge at Fe1 binding a bisphosphine-carborane, and increased charge on Fe2. Compounds **11–12**, which hold a nitrogen or phosphine ligand only at one iron center, had less positive charge on Fe2. Significant negative charge on the terminal CO ligands was enhanced in **16–18** by the CN^- ligands. The other terminal ligands including the phosphine groups carried significant positive charge in **8–15**. Almost one negative charge was located on the CN^- ligands in **16–18**. The bridging CO ligands in **1**, the diamino bridge in **7**, and the dithiolate bridges in **16–18** showed enhanced negative charge, while smaller negative charge was calculated for the bridging ligands of the other compounds. The phosphine or CN^- ligands in **8–10** and **16–18** thus result in a slight apparent reduction of iron, while asymmetric ligation leads to an unequal charge distribution on the metal centers.

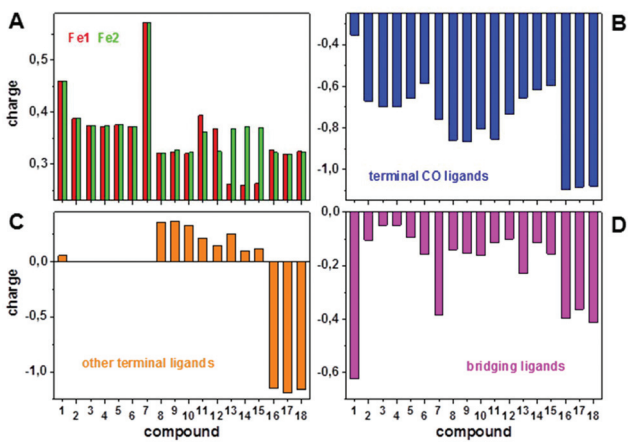

Fig. 9 Charge distribution in **1–18** from DFT. CM5 charges are for relaxed structures (Fig. S5 and S6†). (A) Fe1 and Fe2 charges (left or right iron ions in Fig. 2). (B) Summed charge of terminal CO ligands. (C) Summed charge of remaining ligands. (D) Summed charge of bridging ligands.

Valence level configuration

Calculated HOMOs and LUMOs are shown in Fig. 10. In most cases, the HOMO was dominated by iron contributions (>50%). In the symmetric compounds with mostly CO ligands, extensive HOMO delocalization over both iron ions was observed whereas increasingly asymmetric ligation caused localization on Fe1 or Fe2. The LUMO in most cases was also dominated by iron and delocalized over both centers in the more symmetric complexes, while it was increasingly localized at Fe1 or Fe2 and showed larger ligand contributions in the asymmetric complexes (**13–15**). We estimated experimental LUMO and HOMO energies from the lowest- or highest-energy inflection points of the ctv or vtc spectra (*i.e.* from the respective zero-crossing points in the 2nd-derivative spectra, Fig. S10†). The experimental and calculated LUMO–HOMO energy differences (ΔE) varied by ~0.7 eV for a calculated mean ΔE ~2.3 eV. The ~1 eV smaller experimental mean ΔE may reflect systematic underestimation by the experimental estimation approach (see above), overestimation by DFT (possibly in part due to small contributions of core hole potential differences in the XAS and XES calculations to the frontier MO energy differences), or a combination of both effects (Fig. 11). The correlation between calculated and experimental ΔE values was relatively weak. It became accessible only due to the use of a comparably large number of compounds in the analysis. The calculated HOMO energy varied between about −4 eV (in **18**) and −6 eV (in **2**) and the LUMO energy varied between −2 eV (in **18**) and −4 eV (in **2**), revealing that the more symmetric compounds had relatively lower HOMO/LUMO energies (Table 2).

From the DFT data, 20 unoccupied or occupied MOs of Fe1 and Fe2 with predominantly Fe(d) character were identified (Fig. S8†). They were delocalized over Fe1 and Fe2 in the most symmetric compounds and showed increasing localization for increasing ligation asymmetry. Moderate changes (<0.5 eV) in mean relative energies (about 2 eV and −1 eV) of unoccupied and occupied Fe(d) MOs were observed (Fig. S8†). Although all compounds have 5-coordinated iron ions (except **1** with four ligands), the d-level degeneracy was closer to that of octahedral species with a clear separation of $3t_{2g}$ and $2e_g$ levels, suggesting significant Fe–Fe bonding. Calculated LUMO–HOMO energy differences (ΔE) and energy ranges (corresponding to the apparent d-level degeneracy), total Fe(d) characters, and specific contributions from Fe1/Fe2 to the MOs are

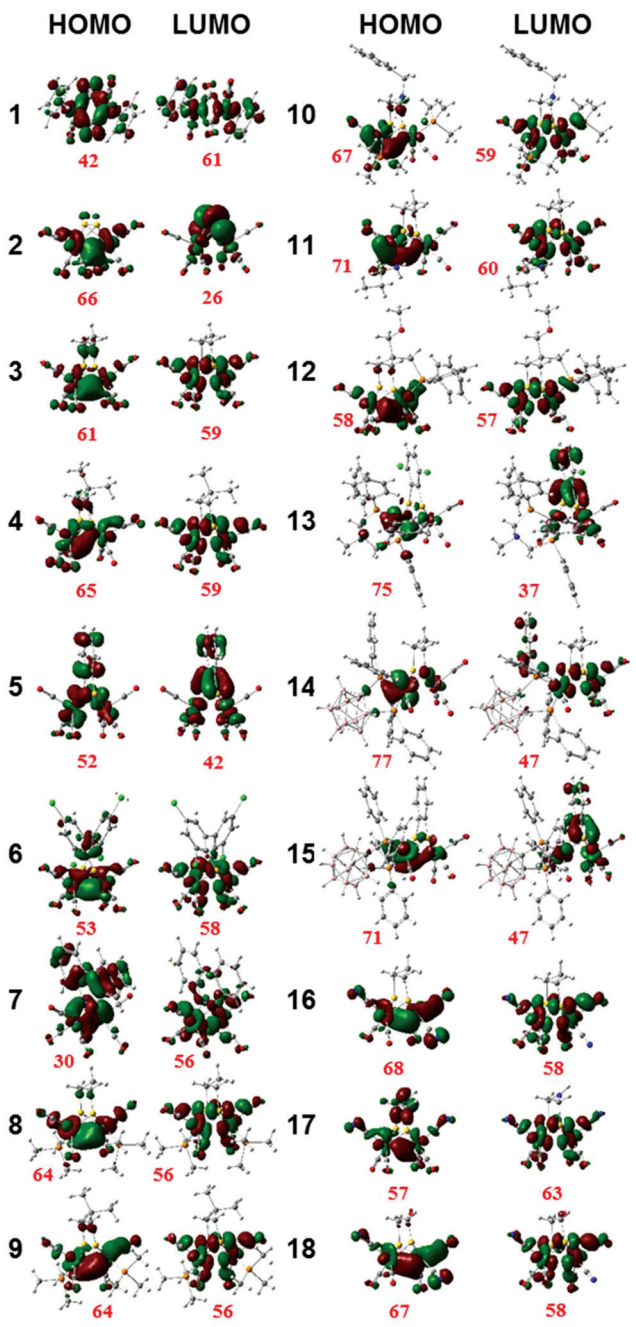

Fig. 10 HOMO and LUMO for **1–18**. Red numbers, total Fe contribution (in %) to MOs (α and β spin MOs are at the same energy and therefore identical for the structures with a total spin of zero due to anti-ferromagnetic coupling of the two Fe(I) ions).

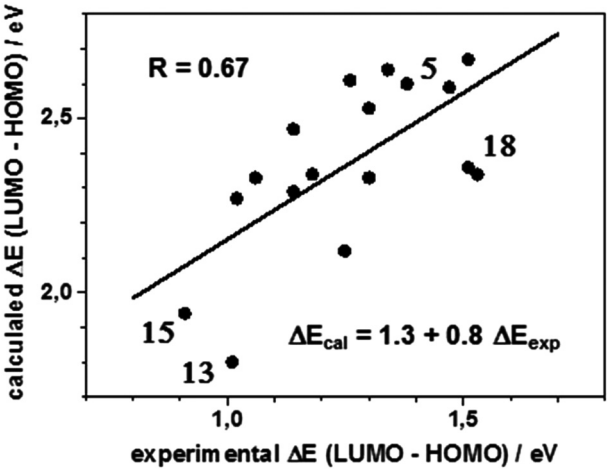

Fig. 11 Frontier MO energy differences in **1–18**. Calculated *vs.* experimental LUMO–HOMO energy differences, solid circles; linear regression, line (for details see the text).

Table 2 Valence level energies and characters of **1–18** from DFT calculations

	Energy [eV]			Energy range[b] [eV]		Fe character[c] [%]		Fe(d) character[d] [%]	
Compound	LUMO	HOMO	ΔE[a] [eV]	Occ. MOs	Unocc. MOs	Occ. MOs	Unocc. MOs	Fe1	Fe2
1	−2.84	−4.81	1.97	1.87	0.75	65.9	53.9	50.0	50.0
2	−3.62	−6.23	2.61	0.68	0.30	66.2	42.3	54.2	53.4
3	−3.23	−5.90	2.67	1.23	0.59	61.9	45.5	54.1	55.1
4	−3.24	−5.88	2.64	1.19	0.57	62.2	45.5	68.7	68.2
5	−3.45	−6.04	2.59	0.72	0.71	57.6	43.9	56.1	56.1
6	−3.73	−6.00	2.27	1.24	0.44	51.8	43.4	55.1	52.5
7	−3.26	−5.86	2.60	0.74	0.46	61.4	37.2	56.2	55.0
8	−2.20	−4.68	2.47	0.90	0.57	59.8	45.4	59.1	56.1
9	−2.19	−4.52	2.33	1.01	0.61	59.8	45.3	57.5	56.1
10	−2.19	−4.52	2.33	0.89	0.62	56.2	41.7	82.7	72.3
11	−2.66	−4.96	2.29	1.10	0.55	63.3	49.2	70.0	62.6
12	−2.71	−5.04	2.34	0.92	0.75	60.9	37.5	70.4	73.4
13	−2.91	−4.70	1.80	1.17	0.79	56.1	39.6	78.3	71.6
14	−2.88	−4.99	2.12	1.03	0.67	60.1	32.2	76.5	67.7
15	−3.05	−4.99	1.94	1.06	0.74	57.2	37.5	73.8	63.5
16	−1.80	−4.15	2.36	0.96	0.52	58.1	43.0	72.5	71.8
17	−1.81	−4.34	2.53	0.74	0.36	54.8	44.0	56.5	56.3
18	−1.70	−4.03	2.34	0.97	0.50	58.5	43.3	72.6	73.8

[a] LUMO–HOMO energy differences. [b] Energy difference between highest- and lowest-energy occupied (occ, 7 MOs) or unoccupied (unocc, 3 MOs) orbitals with predominant Fe(d) character (apparent valence level "degeneracy"). [c] Mean Fe contribution to occ. or unocc. MOs. [d] Mean Fe(d) contribution from Fe1 or Fe2 (left or right iron ion in Fig. 2) to Fe-character of the 10 MOs. Relative energies, Fe characters, and Fe1/Fe2 contributions for the 10 individual MOs shown in Fig. S8.

summarized in Table 2. Smallest or largest ΔE values were found for the most asymmetric (**13**, **15**) or symmetric complexes, regardless of CO to CN^- ligand exchange (*i.e.* in **3** *vs.* **17**). The energy range varied by ~1.2 eV and ~0.6 eV (except for complex **1**) for occupied or unoccupied Fe(d) levels. In particular the most asymmetric compounds with bulky ligands (**12–15**) showed decreased Fe(d) degeneracy. The Fe-character of occupied/unoccupied MOs varied within ~52–66/32–54% with larger contributions for very symmetric compounds. Similar specific Fe1/Fe2 characters of Fe(d) MOs were observed in the more symmetric compounds (**1–9**, **16–18**) whereas Fe1/Fe2 characters deviated by up to ~10% in the more asymmetric compounds (**10–15**).

Structural and electronic parameter relations

Detailed comparison of experimental and calculated parameters related to iron properties such as Fe–Fe distance and Fe charge, valence level energies (HOMO/LUMO, vtc/ctv, and $K\beta_{1,3}$/K-edge energies), and Fe(d) degeneracy/localization (Table 1, 2 and Table S4; Fig. S9†) allowed us to identify four main groups within the 16 compounds bearing a dithiolate bridge (**3–6**, **8–12**, **13–15**, **16–18**), revealing four primary effects in response to ligand exchange *vs.* **2**. For the hexacarbonyl compounds **3–6**, increasingly complex dithiolate bridge decorations mainly result in a shortening of the Fe–Fe distance in comparison to **2**. For compounds **8–12**, CO to phosphine exchange mainly leads to a decrease of the charge on iron compared to the previous group. For compounds **13–15**, CO to bisphosphine-carborane group exchange at one iron center diminishes the degeneracy (*i.e.* increases the energy differences) and localization of Fe(d)-character valence levels *vs.* **2**. For compounds **16–18**, CO to CN^- exchange at both iron centers has the most pronounced effect on the diiron core and, in particular, is increasing the HOMO/LUMO energies. Compound **17** with a nitrogen bridgehead atom shows the strongest deviation of the four properties.

Discussion and conclusions

We report a systematic XAS/XES and DFT study on a broad series of diiron-dithiolate model compounds of the [FeFe]-hydrogenase active site. This approach has further established the sensitivity of K-edge and pre-edge (ctv) absorption spectra and of Kβ main-line and satellite-line (vtc) emission spectra for spin state determination and detection of electronic changes in response to ligation variations at the low-spin Fe(I)Fe(I) centers. The DFT level of theory (BP86/TZVPP) yielded reasonable agreement of experimental and calculated parameters, thereby providing electronic excitation/decay transitions, charge distributions, and valence level configurations. Taking into account the relatively small energy and intensity changes of the ctv and vtc features among the compounds, revealing of correlations between the structural and electronic features has only become feasible due to the use of a large and homogeneous series of diiron compounds in the analysis. Mutual benchmarking of experimental and theoretical XAS/XES data is versatile for prediction and verification of effects of ligation changes on structural, electronic, and spectroscopic properties of diiron compounds in the solid state, as well as in solution, to monitor rotational isomers, redox changes, and protonation events.[38,69,74]

Our data show that four main effects on the diiron core, namely alteration of the Fe–Fe bond length, iron charge, valence level degeneracy/localization, and frontier MO energies, can be preferentially related to changes involving either the dithiolate bridge or the terminal ligands (Fig. 12). Derivatization of the dithiolate bridge, as, for example, in **5**, which has an electron-withdrawing benzene-1,2-dithiolate bridge, *vs.* **3** having a 1,3-propanedithiolate bridge, shortens the Fe–Fe distance, *i.e.* alters the Fe–Fe bond strength, as the main effect. Related changes in metal–metal bonding electron density could be decisive for biasing protonation to this bond or to alternative sites, thereby affecting the probability of bridging hydride formation.[18,37,40,43,44,69] Substitution of CO by more potent electron donors (*e.g.* phosphine ligands) decreased the charge on iron *vs.* the parent hexacarbonyl compounds, as expected, which may decrease the required potential for metal-centered redox reactions.[18] Asymmetric ligand exchange, including electron-donating bisphosphine-carborane groups, caused charge differences at the two iron centers, enhanced valence level delocalization, and HOMO–LUMO gap narrowing, which may facilitate localized redox reactions at less negative potentials to yield mixed-valence species.[68,92–98] Such diiron site species are important in the catalytic cycle of [FeFe]-hydrogenases. CN^- *vs.* CO exchange at both iron centers altered most diiron core properties significantly, decreasing the metal charge, favoring valence delocalization, and increasing frontier MO energies (for example in **16** *vs.* **3**). For this exchange, which conserves the overall geometry of compounds **16–18** in comparison to **2** with six carbonyl ligands, the combined effects on the diiron core are expected to alter both redox and protonation properties.[48,99–102] These considerations may provide further rationales for the synthesis of related diiron compounds as well as for experimental and computational evaluation of their features.

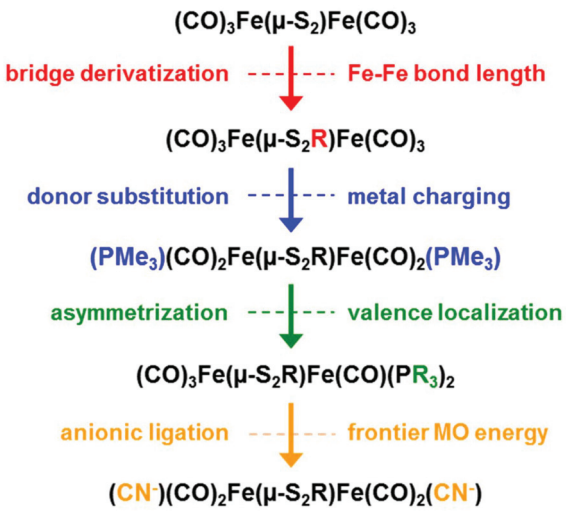

Fig. 12 Effects on the diiron core caused by different ligand variations. Indicated alterations in the coordination sphere (left) of one or both iron centers (middle) lead to indicated main changes at the Fe(I) centers (right). The scheme summarizes our central findings, for further details see text and ESI.†

The diiron site in [FeFe]-hydrogenases shows one terminal CO and one CN^- ligand at each iron center, bridging CO and azadithiolate groups, and asymmetric metal coordination (see Fig. 1). Apo-protein can be converted to the functional enzyme upon binding of **17** to the pre-assembled cubane, release of one CO, and CO rotation into the bridging position.[12,103–108] Compound **17** thereby becomes a superior H_2 conversion catalyst, but reconstitution of [FeFe]-hydrogenases with other diiron compounds (*e.g.* **16**, **18**) has so far not yielded comparable catalytic activity.[12,105,109–111] The low activities, at least in part, reflect perturbed proton conduction to the active site for exchange of the bridgehead amine.[112] CN^- binding and asymmetric metal sites in the native enzyme resemble the properties of, *e.g.*, **13–15** and **16–18**, so that similar effects on the diiron core may be expected. Investigations on [FeFe]-hydrogenases have indeed revealed stabilization of mixed-valence diiron species, biasing of surplus electrons to the diiron or cubane moiety, protonation at the Fe–Fe bond or at the apical vacancy upon reduction due to rotational mobility of diatomic ligands, and decreased frontier MO energy differences compared to diiron compounds.[36,38,74,113–117] A combination of asymmetric metal ligation by anionic, protonable, and electron-delocalizing groups is presumably beneficial for the design of improved diiron hydrogen-conversion catalysts.

Abbreviations

ctv/vtc	Core/valence-to-valence/core transitions
DFT	Density functional theory
EXAFS	Extended X-ray absorption fine structure
HOMO	Highest (energy) occupied MO
LUMO	Lowest (energy) unoccupied MO
MO	Molecular orbital
XANES	X-ray absorption near-edge structure
XAS/XES	X-ray absorption/emission spectroscopy

Author contributions

RK, SM, NS, NL, LS, MK, FW, DD performed research; RK, SM, MH analyzed data; RK, AG, UPA, FG, SO, MH designed research; RK, MH wrote the paper.

Conflicts of interest

There are no conflicts to declare.

Acknowledgements

M. H. thanks the Bundesministerium für Bildung und Forschung (Grant 05 K14KE1) and the Deutsche Forschungsgemeinschaft (DFG) (Grant Ha3265/6-1) for

funding. U.-P. A. thanks the DFG for funding (Emmy Noether Grant AP242/2-1). We thank the team of P. Glatzel at ID26 of ESRF for excellent technical support, S. Ezzaher (Uppsala) for synthesis contributions, and C.-H. Hsieh (laboratory of M. Darensbourg, Texas A & M University, USA) for the generous donation of compounds.

References

1 J. Rifkin, *The Hydrogen Economy*, Tarcher Penguin, New York, 2002.
2 L. Barreto, A. Makihira and K. Riahi, *Int. J. Hydrogen Energy*, 2003, **28**, 267–284.
3 U. Bossel, B. Eliasson and G. Taylor, *Cogener. Compet. Power J.*, 2003, **18**, 29–70.
4 V. Artero, G. Berggren, M. Atta, G. Caserta, S. Roy, L. Pecqueur and M. Fontecave, *Acc. Chem. Res.*, 2015, **48**, 2380–2387.
5 T. B. Rauchfuss, *Science*, 2007, **316**, 553–554.
6 M. Y. Darensbourg, *Nature*, 2005, **433**, 589–591.
7 A. Bachmeier and F. Armstrong, *Curr. Opin. Chem. Biol.*, 2015, **25**, 141–151.
8 W. Lubitz, H. Ogata, O. Rudiger and E. Reijerse, *Chem. Rev.*, 2014, **114**, 4081–4148.
9 J. W. Peters, G. J. Schut, E. S. Boyd, D. W. Mulder, E. M. Shepard, J. B. Broderick, P. W. King and M. W. Adams, *Biochim. Biophys. Acta*, 2015, **1853**, 1350–1369.
10 S. T. Stripp and T. Happe, *Dalton Trans.*, 2009, 9960–9969.
11 A. Silakov, B. Wenk, E. Reijerse and W. Lubitz, *Phys. Chem. Chem. Phys.*, 2009, **11**, 6592–6599.
12 J. Esselborn, N. Muraki, K. Klein, V. Engelbrecht, N. Metzler-Nolte, U.-P. Apfel, E. Hofmann, G. Kurisu and T. Happe, *Chem. Sci.*, 2016, **7**, 959–968.
13 Y. Nicolet, B. J. Lemon, J. C. Fontecilla-Camps and J. W. Peters, *Trends Biochem. Sci.*, 2000, **25**, 138–143.
14 J. W. Peters, W. N. Lanzilotta, B. J. Lemon and L. C. Seefeldt, *Science*, 1998, **282**, 1853–1858.
15 A. J. Pierik, M. Hulstein, W. R. Hagen and S. P. Albracht, *Eur. J. Biochem.*, 1998, **258**, 572–578.
16 A. L. De Lacey, C. Stadler, C. Cavazza, E. C. Hatchikian and V. M. Fernandez, *J. Am. Chem. Soc.*, 2000, **122**, 11232–11233.
17 T. R. Simmons, G. Berggren, M. Bacchia, M. Fontecave and V. Artero, *Coord. Chem. Rev.*, 2014, **270–271**, 127–150.
18 F. Gloaguen and T. B. Rauchfuss, *Chem. Soc. Rev.*, 2009, **38**, 100–108.
19 M. Y. Darensbourg, E. J. Lyon and J. J. Smee, *Coord. Chem. Rev.*, 2000, **206**, 533–561.
20 C. Tard and C. J. Pickett, *Chem. Rev.*, 2009, **109**, 2245–2274.
21 U. P. Apfel, D. Troegel, Y. Halpin, S. Tschierlei, U. Uhlemann, H. Gorls, M. Schmitt, J. Popp, P. Dunne, M. Venkatesan, M. Coey, M. Rudolph, J. G. Vos, R. Tacke and W. Weigand, *Inorg. Chem.*, 2010, **49**, 10117–10132.
22 A. Magnuson, M. Anderlund, O. Johansson, P. Lindblad, R. Lomoth, T. Polivka, S. Ott, K. Stensjo, S. Styring, V. Sundstrom and L. Hammarstrom, *Acc. Chem. Res.*, 2009, **42**, 1899–1909.
23 L. C. Sun, B. Akermark and S. Ott, *Coord. Chem. Rev.*, 2005, **249**, 1653–1663.
24 P. V. Rao and R. H. Holm, *Chem. Rev.*, 2004, **104**, 527–559.
25 M. Wang, L. Chen, X. Li and L. Sun, *Dalton Trans.*, 2011, **40**, 12793–12800.
26 M. Y. Darensbourg and R. D. Bethel, *Nat. Chem.*, 2012, **4**, 11–13.
27 D. Schilter, J. M. Camara, M. T. Huynh, S. Hammes-Schiffer and T. B. Rauchfuss, *Chem. Rev.*, 2016, **116**, 8693–8749.
28 R. D. Bethel and M. Y. Darensbourg, in *Bioorganometallic Chemistry: Applications in Drug Discovery Biocatalysis, and Imaging*, ed. G. Jaouen and M. Salmain, Wiley-VCH, Weinheim, 2014, pp. 239–272.
29 D. J. Evans and C. J. Pickett, *Chem. Soc. Rev.*, 2003, **32**, 268–275.
30 D. M. Heinekey, *J. Organomet. Chem.*, 2009, **694**, 2671–2680.
31 S. Tschierlei, S. Ott and R. Lomoth, *Energy Environ. Sci.*, 2011, **4**, 2340–2352.
32 F. Gloaguen, *Inorg. Chem.*, 2016, **55**, 390–398.
33 Y. L. Li and T. B. Rauchfuss, *Chem. Rev.*, 2016, **116**, 7043–7077.
34 C. Lambertz, N. Leidel, K. G. Havelius, J. Noth, P. Chernev, M. Winkler, T. Happe and M. Haumann, *J. Biol. Chem.*, 2011, **286**, 40614–40623.
35 K. D. Swanson, M. W. Ratzloff, D. W. Mulder, J. H. Artz, S. Ghose, A. Hoffman, S. White, O. A. Zadvornyy, J. B. Broderick, B. Bothner, P. W. King and J. W. Peters, *J. Am. Chem. Soc.*, 2015, **137**, 1809–1816.
36 D. W. Mulder, Y. Guo, M. W. Ratzloff and P. W. King, *J. Am. Chem. Soc.*, 2016, **139**, 83–86.
37 G. Filippi, F. Arrigoni, L. Bertini, L. De Gioia and G. Zampella, *Inorg. Chem.*, 2015, **54**, 9529–9542.
38 P. Chernev, C. Lambertz, A. Brunje, N. Leidel, K. G. Sigfridsson, R. Kositzki, C. H. Hsieh, S. Yao, R. Schiwon, M. Driess, C. Limberg, T. Happe and M. Haumann, *Inorg. Chem.*, 2014, **53**, 12164–12177.
39 N. Leidel, C. H. Hsieh, P. Chernev, K. G. Sigfridsson, M. Y. Darensbourg and M. Haumann, *Dalton Trans.*, 2013, **42**, 7539–7554.
40 A. R. Finkelmann, M. T. Stiebritz and M. Reiher, *Chem. Sci.*, 2013, **5**, 215–221.
41 B. E. Barton, G. Zampella, A. K. Justice, L. De Gioia, T. B. Rauchfuss and S. R. Wilson, *Dalton Trans.*, 2010, **39**, 3011–3019.
42 N. Wang, M. Wang, J. Liu, K. Jin, L. Chen and L. Sun, *Inorg. Chem.*, 2009, **48**, 11551–11558.
43 B. E. Barton and T. B. Rauchfuss, *Inorg. Chem.*, 2008, **47**, 2261–2263.
44 S. Loscher, L. Schwartz, M. Stein, S. Ott and M. Haumann, *Inorg. Chem.*, 2007, **46**, 11094–11105.

45 S. Ezzaher, J. F. Capon, F. Gloaguen, F. Y. Petillon, P. Schollhammer, J. Talarmin, R. Pichon and N. Kervarec, *Inorg. Chem.*, 2007, **46**, 3426–3428.
46 L. Schwartz, G. Eilers, L. Eriksson, A. Gogoll, R. Lomoth and S. Ott, *Chem. Commun.*, 2006, 520–522.
47 S. L. Matthews and D. M. Heinekey, *Inorg. Chem.*, 2010, **49**, 9746–9748.
48 T. B. Rauchfuss, *Acc. Chem. Res.*, 2015, **48**, 2107–2116.
49 N. Wang, M. Wang, Y. Wang, D. H. Zheng, H. X. Han, M. S. G. Ahlquist and L. C. Sun, *J. Am. Chem. Soc.*, 2013, **135**, 13688–13691.
50 N. Wang, M. Wang, L. Chen and L. C. Sun, *Dalton Trans.*, 2013, **42**, 12059–12071.
51 S. E. Smith, J. Y. Yang, D. L. DuBois and R. M. Bullock, *Angew. Chem., Int. Ed.*, 2012, **51**, 3152–3155.
52 J. C. Lansing, J. M. Camara, D. E. Gray and T. B. Rauchfuss, *Organometallics*, 2014, **33**, 5897–5906.
53 S. Hammes-Schiffer, *J. Am. Chem. Soc.*, 2015, **137**, 8860–8871.
54 G. Si, W. G. Wang, H. Y. Wang, C. H. Tung and L. Z. Wu, *Inorg. Chem.*, 2008, **47**, 8101–8111.
55 D. W. Yang, Y. Li, B. M. Wang, X. Y. Zhao, L. N. Su, S. Chen, P. Tong, Y. Luo and J. P. Qu, *Inorg. Chem.*, 2015, **54**, 10243–10249.
56 F. A. Armstrong, N. A. Belsey, J. A. Cracknell, G. Goldet, A. Parkin, E. Reisner, K. A. Vincent and A. F. Wait, *Chem. Soc. Rev.*, 2009, **38**, 36–51.
57 M. Haumann, in *Biohydrogen*, ed. M. Rögner, DeGruyter, Berlin, 2015, pp. 97–116.
58 P. Glatzel and U. Bergmann, *Coord. Chem. Rev.*, 2005, **249**, 65–95.
59 F. De Groot and A. Kotani, *Core Level Spectroscopy of Solids*, Taylor & Francis CRC Press, Boca Raton, FL, USA, 2008.
60 B. Kirchner, F. Wennmohs, S. F. Ye and F. Neese, *Curr. Opin. Chem. Biol.*, 2007, **11**, 134–141.
61 P. E. Siegbahn, J. W. Tye and M. B. Hall, *Chem. Rev.*, 2007, **107**, 4414–4435.
62 C. J. Pollock and S. DeBeer, *Acc. Chem. Res.*, 2015, **48**, 2967–2975.
63 U. Bergmann, P. Glatzel, J. H. Robblee, J. Messinger, C. Fernandez, R. Cinco, H. Visser, K. McFarlane, E. Bellacchio, S. Pizarro, K. Sauer, V. K. Yachandra, M. P. Klein, B. L. Cox, K. H. Nealson and S. P. Cramer, *J. Synchrotron Radiat.*, 2001, **8**, 199–203.
64 G. N. George, B. Hedman and K. O. Hodgson, *Nat. Struct. Biol.*, 1998, **5**, 645–647.
65 F. de Groot, *Chem. Rev.*, 2001, **101**, 1779–1808.
66 N. J. Vollmers, P. Muller, A. Hoffmann, S. Herres-Pawlis, M. Rohrmuller, W. G. Schmidt, U. Gerstmann and M. Bauer, *Inorg. Chem.*, 2016, **55**, 11694–11706.
67 J. A. van Bokhoven and C. Lamberti, *X-Ray Absorption and X-Ray Emission Spectroscopy*, Wiley, New York, 2016.
68 S. Yao, F. Meier, N. Lindenmaier, R. Rudolph, B. Blom, M. Adelhardt, J. Sutter, S. Mebs, M. Haumann, K. Meyer, M. Kaupp and M. Driess, *Angew. Chem., Int. Ed.*, 2015, **54**, 12506–12510.
69 N. Leidel, P. Chernev, K. G. Havelius, L. Schwartz, S. Ott and M. Haumann, *J. Am. Chem. Soc.*, 2012, **134**, 14142–14157.
70 N. Leidel, P. Chernev, K. G. Havelius, S. Ezzaher, S. Ott and M. Haumann, *Inorg. Chem.*, 2012, **51**, 4546–4559.
71 C. Colomban, E. V. Kudrik, V. Briois, J. C. Shwarbrick, A. B. Sorokin and P. Afanasiev, *Inorg. Chem.*, 2014, **53**, 11517–11530.
72 J. K. Kowalska, A. W. Hahn, A. Albers, C. E. Schiewer, R. Bjornsson, F. A. Lima, F. Meyer and S. DeBeer, *Inorg. Chem.*, 2016, **55**, 4485–4497.
73 M. Y. Guo, L. K. Sorensen, M. G. Delcey, R. V. Pinjari and M. Lundberg, *Phys. Chem. Chem. Phys.*, 2016, **18**, 3250–3259.
74 C. Lambertz, P. Chernev, K. Klingan, N. Leidel, K. G. V. Siegfridsson, T. Happe and M. Haumann, *Chem. Sci.*, 2014, **5**, 1187–1203.
75 S. Mebs, N. Braun, R. Kositzki, C. Limberg and M. Haumann, *Inorg. Chem.*, 2015, **54**, 11606–11624.
76 A. Petuker, S. Mebs, N. Schuth, P. Gerschel, M. Seidel, B. Mallick, M. van Gastel, M. Haumann and U. P. Apfel, *Dalton Trans.*, 2017, **46**, 907–917.
77 R. Kositzki, S. Mebs, J. Marx, J. J. Griese, N. Schuth, M. Högbom, V. Schünemann and M. Haumann, *Inorg. Chem.*, 2016, **19**, 9869–9885.
78 I. Zaharieva, P. Chernev, G. Berggren, M. Anderlund, S. Styring, H. Dau and M. Haumann, *Biochemistry*, 2016, **55**, 4197–4211.
79 H. Dau, P. Liebisch and M. Haumann, *Anal. Bioanal. Chem.*, 2003, **376**, 562–583.
80 A. D. Becke, *Phys. Rev. A*, 1988, **38**, 3098–3100.
81 J. P. Perdew, *Phys. Rev. B: Condens. Matter*, 1986, **33**, 8822.
82 A. Schäfer, C. Huber and R. Ahlrichs, *J. Chem. Phys.*, 1994, **100**, 5829–5835.
83 F. Neese, *Wiley Interdiscip. Rev.: Comput. Mol. Sci.*, 2012, **2**, 73–78.
84 M. J. T. Frisch, H. B. Schlegel, G. E. Scuseria, M. A. Robb, J. R. Cheeseman, G. Scalmani, V. Barone, B. Mennucci, G. A. Petersson, H. Nakatsuji, M. Caricato, X. Li, H. P. Hratchian, A. F. Izmaylov, J. Bloino, G. Zheng, J. L. Sonnenberg, M. Hada, M. Ehara, K. Toyota, R. Fukuda, J. Hasegawa, M. Ishida, T. Nakajima, Y. Honda, O. Kitao, H. Nakai, T. Vreven, J. A. Montgomery Jr., J. E. Peralta, F. Ogliaro, M. Bearpark, J. J. Heyd, E. Brothers, K. N. Kudin, V. N. Staroverov, R. Kobayashi, J. Normand, K. Raghavachari, A. Rendell, J. C. Burant, S. S. Iyengar, J. Tomasi, M. Cossi, N. Rega, J. M. Millam, M. Klene, J. E. Knox, J. B. Cross, V. Bakken, C. Adamo, J. Jaramillo, R. Gomperts, R. E. Stratmann, O. Yazyev, A. J. Austin, R. Cammi, C. Pomelli, J. W. Ochterski, R. L. Martin, K. Morokuma, V. G. Zakrzewski, G. A. Voth, P. Salvador, J. J. Dannenberg, S. Dapprich, A. D. Daniels, Ö. Farkas, J. B. Foresman, J. V. Ortiz, J. Cioslowski and D. J. Fox, Gaussian, Inc., Wallingford CT, 2009.

85 C. J. Pollock, M. U. Delgado-Jaime, M. Atanasov, F. Neese and S. DeBeer, *J. Am. Chem. Soc.*, 2014, **136**, 9453–9463.
86 X. Wang, F. De Groot and S. P. Cramer, *Phys. Rev. B: Condens. Matter*, 1997, **56**, 4553–4564.
87 M. Salomone-Stagni, F. Stellato, C. M. Whaley, S. Vogt, S. Morante, S. Shima, T. B. Rauchfuss and W. Meyer-Klaucke, *Dalton Trans.*, 2010, **39**, 3057–3064.
88 T. E. Westre, P. Kennepohl, J. G. DeWitt, B. Hedman, K. O. Hodgson and E. I. Solomon, *J. Am. Chem. Soc.*, 1997, **119**, 6297–6314.
89 F. M. de Groot, P. Glatzel, U. Bergmann, P. A. van Aken, R. A. Barrea, S. Klemme, M. Havecker, A. Knop-Gericke, W. M. Heijboer and B. M. Weckhuysen, *J. Phys. Chem. B*, 2005, **109**, 20751–20762.
90 R. Stowasser and R. Hoffmann, *J. Am. Chem. Soc.*, 1999, **121**, 3414–3420.
91 S. N. MacMillan, R. C. Walroth, D. M. Perry, T. J. Morsing and K. M. Lancaster, *Inorg. Chem.*, 2015, **54**, 205–214.
92 J. Rittle, C. C. L. McCrory and J. C. Peters, *J. Am. Chem. Soc.*, 2014, **136**, 13853–13862.
93 W. G. Wang, M. J. Nilges, T. B. Rauchfuss and M. Stein, *J. Am. Chem. Soc.*, 2013, **135**, 3633–3639.
94 P. S. Singh, H. C. Rudbeck, P. Huang, S. Ezzaher, L. Eriksson, M. Stein, S. Ott and R. Lomoth, *Inorg. Chem.*, 2009, **48**, 10883–10885.
95 M. T. Olsen, A. K. Justice, F. Gloaguen, T. B. Rauchfuss and S. R. Wilson, *Inorg. Chem.*, 2008, **47**, 11816–11824.
96 A. K. Justice, L. De Gioia, M. J. Nilges, T. B. Rauchfuss, S. R. Wilson and G. Zampella, *Inorg. Chem.*, 2008, **47**, 7405–7414.
97 A. K. Justice, T. B. Rauchfuss and S. R. Wilson, *Angew. Chem., Int. Ed.*, 2007, **46**, 6152–6154.
98 M. Karnahl, S. Tschierlei, O. F. Erdem, S. Pullen, M. P. Santoni, E. J. Reijerse, W. Lubitz and S. Ott, *Dalton Trans.*, 2012, **41**, 12468–12477.
99 L. C. Song, Z. Y. Yang, H. Z. Bian and Q. M. Hu, *Organometallics*, 2004, **23**, 3082–3084.
100 H. Li and T. B. Rauchfuss, *J. Am. Chem. Soc.*, 2002, **124**, 726–727.
101 B. C. Manor, M. R. Ringenberg and T. B. Rauchfuss, *Inorg. Chem.*, 2014, **53**, 7241–7247.
102 E. J. Lyon, I. P. Georgakaki, J. H. Reibenspies and M. Y. Darensbourg, *Angew. Chem., Int. Ed.*, 1999, **38**, 3178–3180.
103 T. Happe and A. Hemschemeier, *Trends Biotechnol.*, 2014, **32**, 170–176.
104 J. Esselborn, C. Lambertz, A. Adamska-Venkatesh, T. Simmons, G. Berggren, J. Noth, J. Siebel, A. Hemschemeier, V. Artero, E. Reijerse, M. Fontecave, W. Lubitz and T. Happe, *Nat. Chem. Biol.*, 2013, **10**, 607–609.
105 G. Berggren, A. Adamska, C. Lambertz, T. R. Simmons, J. Esselborn, M. Atta, S. Gambarelli, J. M. Mouesca, E. Reijerse, W. Lubitz, T. Happe, V. Artero and M. Fontecave, *Nature*, 2013, **499**, 66–69.
106 R. Gilbert-Wilson, J. F. Siebel, A. Adamska-Venkatesh, C. C. Pham, E. Reijerse, H. Wang, S. P. Cramer, W. Lubitz and T. B. Rauchfuss, *J. Am. Chem. Soc.*, 2015, **137**, 8998–9005.
107 A. Adamska-Venkatesh, T. R. Simmons, J. F. Siebel, V. Artero, M. Fontecave, E. Reijerse and W. Lubitz, *Phys. Chem. Chem. Phys.*, 2015, **17**, 5421–5430.
108 M. Senger, S. Mebs, J. Duan, F. Wittkamp, U. P. Apfel, J. Heberle, M. Haumann and S. T. Stripp, *Proc. Natl. Acad. Sci. U. S. A.*, 2016, **113**, 8454–8459.
109 C. F. Megarity, J. Esselborn, S. V. Hexter, F. Wittkamp, U. P. Apfel, T. Happe and F. A. Armstrong, *J. Am. Chem. Soc.*, 2016, **138**, 15227–15233.
110 J. F. Siebel, A. Adamska-Venkatesh, K. Weber, S. Rumpel, E. Reijerse and W. Lubitz, *Biochemistry*, 2015, **54**, 1474–1483.
111 A. Adamska-Venkatesh, D. Krawietz, J. Siebel, K. Weber, T. Happe, E. Reijerse and W. Lubitz, *J. Am. Chem. Soc.*, 2014, **136**, 11339–11346.
112 M. Winkler, J. Esselborn and T. Happe, *Biochim. Biophys. Acta*, 2013, **1827**, 974–985.
113 Z. P. Liu and P. Hu, *J. Am. Chem. Soc.*, 2002, **124**, 5175–5182.
114 A. Adamska, A. Silakov, C. Lambertz, O. Rudiger, T. Happe, E. Reijerse and W. Lubitz, *Angew. Chem., Int. Ed.*, 2012, **51**, 11458–11462.
115 A. Silakov, B. Wenk, E. Reijerse, S. P. Albracht and W. Lubitz, *J. Biol. Inorg. Chem.*, 2009, **14**, 301–313.
116 A. Silakov, E. J. Reijerse, S. P. Albracht, E. C. Hatchikian and W. Lubitz, *J. Am. Chem. Soc.*, 2007, **129**, 11447–11458.
117 V. Fourmond, C. Greco, K. Sybirna, C. Baffert, P. H. Wang, P. Ezanno, M. Montefiori, M. Bruschi, I. Meynial-Salles, P. Soucaille, J. Blumberger, H. Bottin, L. De Gioia and C. Leger, *Nat. Chem.*, 2014, **6**, 336–342.
118 A. Mitschler, B. Rees and M. S. Lehmann, *J. Am. Chem. Soc.*, 1978, **100**, 3390–3397.
119 I. L. Eremenko, H. Berke, A. A. H. Vanderzeijden, B. I. Kolobkov and V. M. Novotortsev, *J. Organomet. Chem.*, 1994, **471**, 123–132.
120 M. L. Singleton, R. M. Jenkins, C. L. Klernashevich and M. Y. Darensbourg, *Cron. Chim.*, 2008, **11**, 861–874.
121 J. A. Cabeza, M. A. Martinez-Garcia, V. Riera, D. Ardura and S. Garcia-Granda, *Organometallics*, 1998, **17**, 1471–1477.
122 L. Schwartz, P. S. Singh, L. Eriksson, R. Lomoth and S. Ott, *Cron. Chim.*, 2008, **11**, 875–889.
123 K. Charreteur, M. Kdider, J. F. Capon, F. Gloaguen, F. Y. Petillon, P. Schollhammer and J. Talarmin, *Inorg. Chem.*, 2010, **49**, 2496–2501.
124 R. J. Doedens, *Inorg. Chem.*, 1970, **9**, 429–436.
125 X. Zhao, I. P. Georgakaki, M. L. Miller, J. C. Yarbrough and M. Y. Darensbourg, *J. Am. Chem. Soc.*, 2001, **123**, 9710–9711.
126 M. L. Singleton, N. Bhuvanesh, J. H. Reibenspies and M. Y. Darensbourg, *Angew. Chem., Int. Ed.*, 2008, **47**, 9492–9495.

127 L. Schwartz, J. Ekstrom, R. Lomoth and S. Ott, *Chem. Commun.*, 2006, 4206–4208.
128 D. Daunke, *Metallkomplexe polypodaler Thiolatliganden als Modellsysteme für FeFe- und FeNi-Hydrogenasen*, *Ph.D. Thesis*, Technische Universität Berlin, Berlin, 2014.
129 S. Ezzaher, A. Gogoll, C. Bruhn and S. Ott, *Chem. Commun.*, 2010, **46**, 5775–5777.
130 M. Schmidt, S. M. Contakes and T. B. Rauchfuss, *J. Am. Chem. Soc.*, 1999, **121**, 9736–9737.
131 C. R. Groom, I. J. Bruno, M. P. Lightfoot and S. C. Ward, *Acta Crystallogr., Sect. B: Struct. Sci.*, 2016, **72**, 171–179.